Schweizerischer Erdbebendienst
Service Sismologique Suisse
Servizio Sismico Svizzero
Swiss Seismological Service

ETH
Eidgenössische Technische Hochschule Zürich
Swiss Federal Institute of Technology Zurich

SITE CHARACTERIZATION REPORT

SONUG: Geneva (GE)

Francesco Panzera, Dario Chieppa, Donat Fäh

Last Modification: 01st March, 2022

Schweizerischer Erdbebendienst (SED)
Service Sismologique Suisse
Servizio Sismico Svizzero
Servizi da Terratrembels Svizzer

ETH Zürich
Sonneggstrasse 5
8092 Zürich Schweiz
francesco.panzera@sed.ethz.ch

Contents

Summary

The SSMNet station SONUG was installed 31.10.2019 in the City of Geneva (GE) inside the United Nations Office. From a geological point of view, the station is located on Moraine deposits overlaying conglomerates which are exposed 50 m far on the North-Western direction with respect the station position. Active seismic measurements, as well as single-station ambient vibration measurement, were performed to investigate the subsurface structure beneath the station. The site is characterized by a low amplitude fundamental frequency peak at about 0.75 Hz, which can be related to an interface between rock formations, well beyond the investigation depth reached by our measurements (which is approximately 20-40 m). Moreover, the HVSR shows a high frequency peak at 9.5 Hz, which can be associated to a thin low velocity layer. The estimated V_{S30} value is 627 m/s, which classifies the site as E type in SIA261 (SIA, 2014) and class B in the Eurocode 8 (CEN, 2004).

1 Introduction

The station SONUG is part of the Swiss Strong Motion Network (SSMNet). The station has been installed on 31.10.2019 in the framework of the second phase of the Swiss Strong Motion Network (SSMNet) renewal project (Fig. 1). In order to better characterize the subsurface at the station, we performed an active seismic survey and single station measurements of ambient vibrations.
The site is located in Western Switzerland at the border with France and its geographical location improves the network coverage of the area.
The measurement campaign was carried out on 08.09.2021 in order to characterize the soil column in terms of fundamental frequency and shear wave velocity.

Figure 1: Map showing the location of the strong motion station (white triangle) in Geneva. © 2019 swisstopo (JD100042)

2 Geological setting

A geological map of the surroundings of the site in Geneva is shown in Fig. 2 The seismic station SONUG is located on moraine deposit overlaying conglomerates which outcrop in the NW area. In the Eastern part is instead outcropping an artificial deposit.
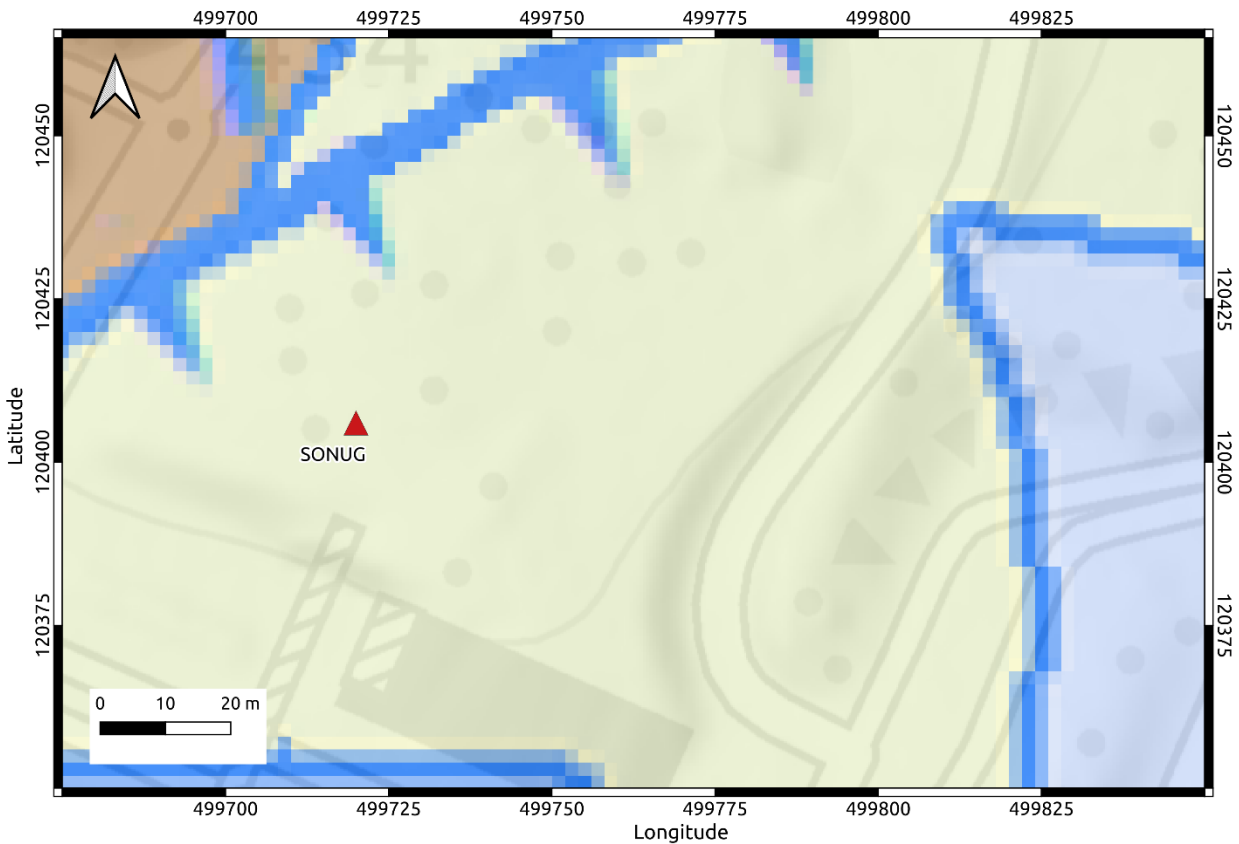
Figure 2: Geological map of the SONUG seismic station area identified by a red triangle. light blue area = artificial deposits; Light green = moraine; brown area = conglomerates. © 2019 swisstopo (JD100042)

3 Active seismic measurements and processing

The active seismic line was deployed close to SONUG (about 30 m far), along a NE-SW direction (Figure 3). For the sake of a comprehensive subsurface characterization, multichannel analysis of surface waves (MASW; Park et al., 1999) survey was conducted.

3.1 Equipment

We used three sets of 8 three-component geophones (4.5 Hz corner frequency). Each geophone set was connected to a Geode datalogger; the three Geodes were coupled for time synchronization. The seismic source was a 5-kg sledgehammer, hitting a flat metal plate at two source locations (yellow stars in Figure 3) outside the geophone line.

The synchronization between the traces recorded by the geophones and the seismic source was ensured by a trigger device fastened to the hammer handle.
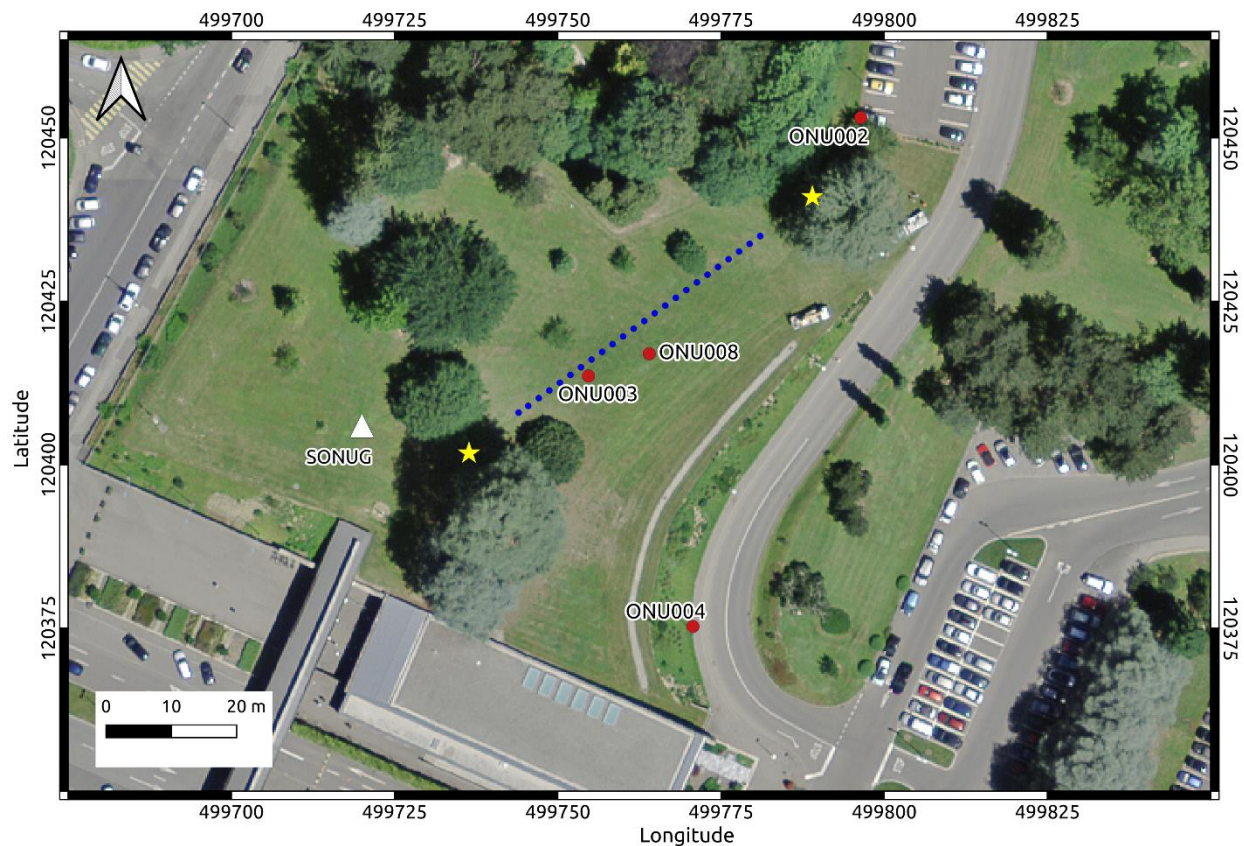
Figure 3: Map representing the position of the targeted station (SONUG, white triangle), of the active seismic line (yellow stars – sources, blue circles - geophones) and of the noise recording sensors (reds circles).

3.2 Geometry of the acquisition array

The seismic line was constituted by 24 three-component receivers aligned at regular intervals of 2 m, for a total length of 46 m. The geophones were laid on the soil with metal spikes ensuring a firm coupling with the ground.

As earlier anticipated, MASW was performed placing the sources at two locations 10 m from the closest geophone: at the NE end, and at the SW end (Figure 3). At these shooting positions the sledgehammer was vertically blown on a flat metal plate (Figure 3) for Rayleigh wave generation.

Figure 4: Geophone array in place. The picture was taken near the SW end of the line (view point SW to NE).

3.3 Acquisition

The time-sampling parameters adopted for MASW was the following: sampling interval = 0.5 ms, record length = 3 s, pre-trigger delay = -0.1 s.

At the source points, 10 hammer shots were blown and the traces generated were saved in separated .sg2 file (without automatic stack). In Figure 5 we show sample seismic sections from Rayleigh wave shots.
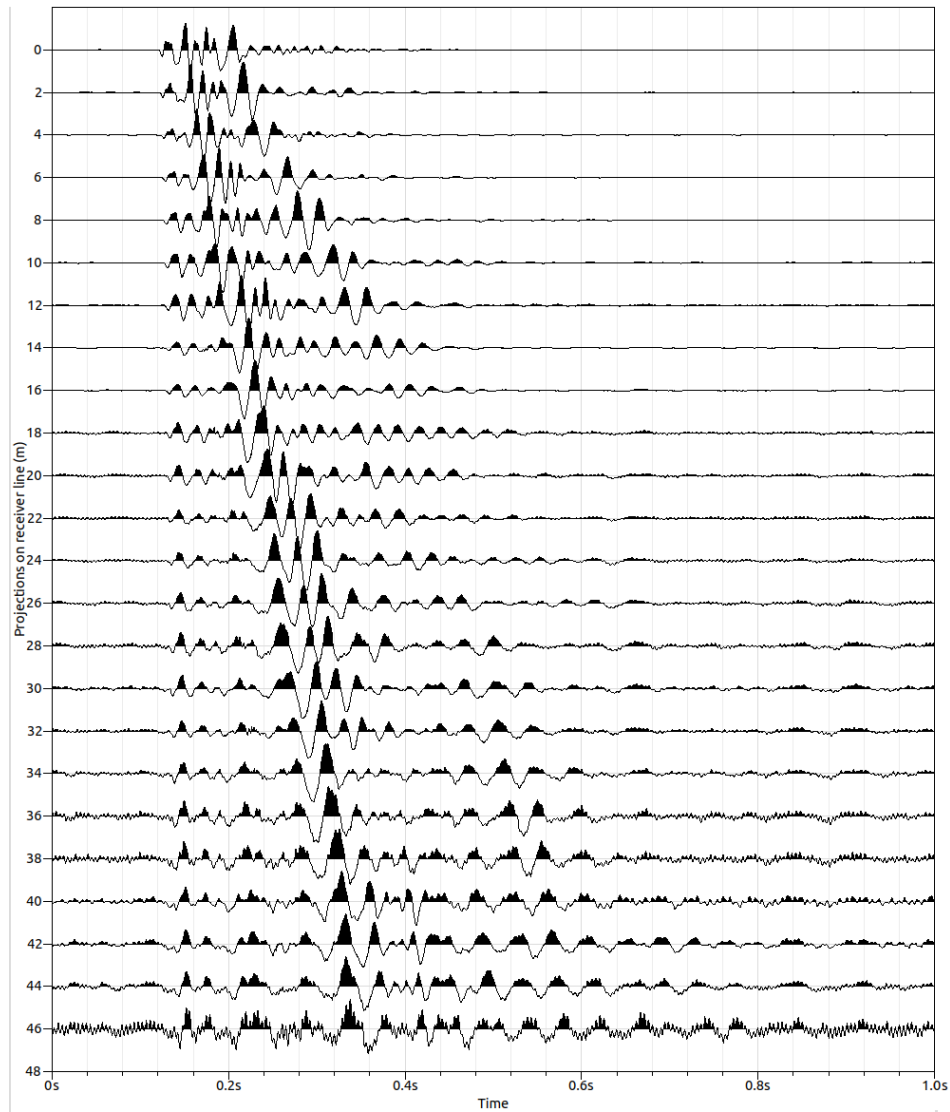
Figure 5: Examples of acquired seismic sections from vertical component wave shot.

3.4 Processing

3.4.1 Rayleigh wave data *f-k* processing

Rayleigh wave dispersion characteristic were extracted from the vertical component seismograms from MASW acquisitions. The considered seismic sections were processed by means of *f-k* (frequency – wavenumber) transform (Kvaerna and Ringdahl, 1986), in order to obtain a conversion of the recorded sets of traces from time–offset to frequency–wavenumber domain and then dispersion curves of Rayleigh waves. The Rayleigh wave dispersion curve panels from single shot records with the same source position were summed to obtain spectral images with greater S/N ratio (O'Neill, 2003; Neducza, 2007). The energy maxima in the Rayleigh wave dispersion curves were picked on these stacked panels; spectral amplitude peaks from individual shot recordings were identified as well, and used to define the uncertainty intervals in the estimation of phase velocities (Socco et al., 2009; Boiero and Socco, 2010).

Figure 6 shows the stacked dispersion curves panels from the considered seismic records, as well as the corresponding picked energy maxima. The dominant feature in both spectra considering the shot in the NE and SW position is a branch extending continuously in the 16-73 Hz frequency band. This feature is to be associated with the fundamental mode of Rayleigh wave propagation. Other branches at higher frequencies are not visible or distinguishable.
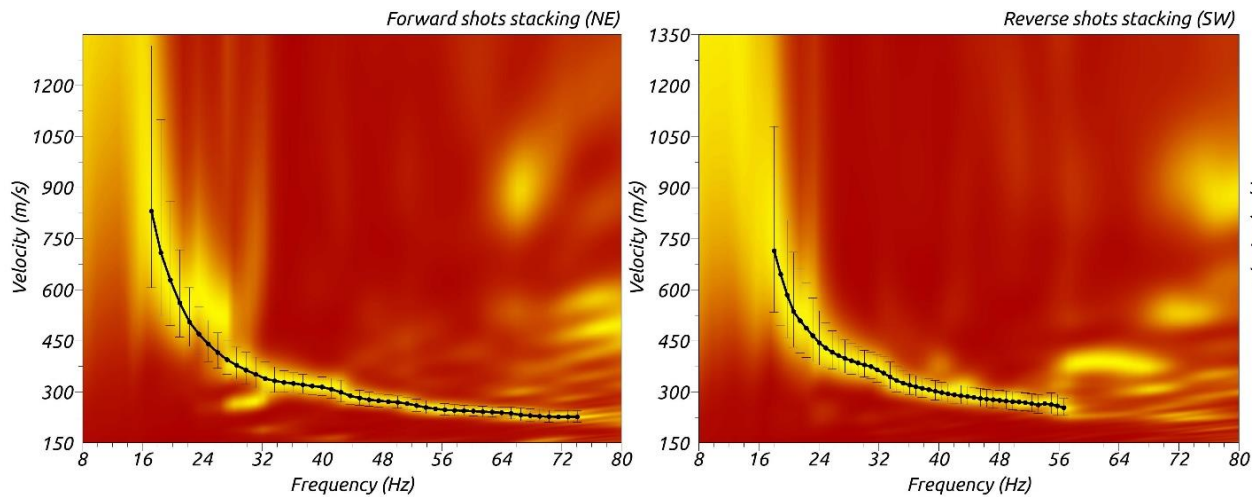
Figure 6: Phase velocity versus frequency stacked spectra obtained considering the recordings from the two shot points at the NE and SW ends of the deployments.

4 Passive seismic measurements

4.1 Acquisition and equipment

Beside the active seismic survey, two single-station noise recording measurements were performed on the same acquisition day and others three in 2017 ONU002, ONU003 and ONU004 (see location in Fig. 3). One measurement was performed just few meters from SONUG, but the station did not work properly. A second measurement ONU008 (see location in Fig. 3) was made near the active seismic line. In all cases, the sensor (Lennartz 3C 5s seismometer) was placed on a metal tripod in contact with the ground (Figure 7). The sampling frequency was 200 Hz and the recording spanned a 40-minute time interval; a Centaur datalogger was employed.

Figure 7 – Single-station ambient vibration recording ONU008 performed nearby the center of the linear deployment for MASW.

4.2 Single station processing

The passive traces were processed with the aim of:

- estimating the H/V ratio of recorded noise, thus identifying the fundamental frequency of resonance of the site (Nakamura, 1989) by the use of classical H/V methods (as implemented in Geopsy software, www. geopsy.org; classical H/V of Fäh et al., 2001).
- estimating the ellipticity of Rayleigh wave as a function of frequency by resorting to refined algorithms (Raydec, Hobiger at al., 2009; time-frequency method, Poggi and Fäh, 2010; wavelet-based time-frequency method as implemented in Geopsy software).

To obtain a more reliable estimation of Rayleigh wave ellipticity the latter methods aim at eliminating the contributions of other waves besides Rayleigh waves, when compared to the classical H/V technique.

The results are shown in Figure 8. All applied techniques yield similar H/V or ellipticity curves, with a bimodal low frequency peak in between 0.4 and 1.0 Hz and a secondary peak at about 9.5 Hz. The low frequency bimodal peak could be explained as the resonance of Molasse deposits having thickness in Geneva basin of about 1000 m (Moscariello, 2019), whereas the high frequency peak could be related to the artificial deposits outcropping in the area.

To verify if the thickness of the sedimentary cover is homogeneous around the station we overplotted together all the H/V curves coming from Classical 1 method (Fig. 8). Moreover, having not a H/V nearby the SMNET station we computed H/V using 1-hour signal extracted from the SONUG accelerometer station. All the curves are in agreement at frequency above 1.0 Hz, whereas below 1.0 Hz due to accelerometer sensitivity the H/V at the station SONUG is flat and not able to reproduce the bimodal low frequency peak. The results suggest that the thickness of the uppermost part of the sedimentary cover is almost the same in the investigated area.
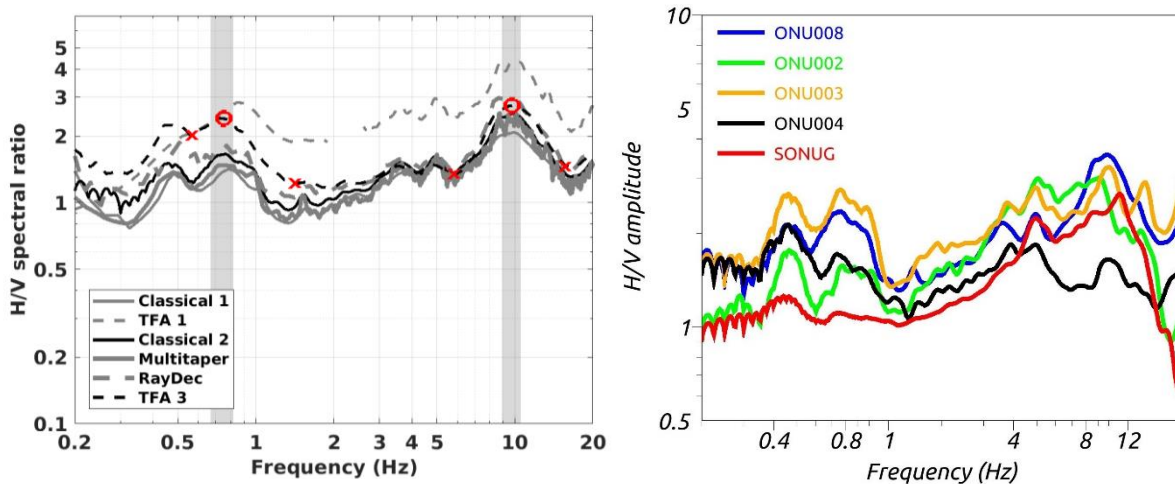
Figure 8 – H/V ratio and ellipticity curves obtained from the processing of noise recording data, using several algorithms at the sites ONU008 (left panel) and comparison of the H/V curves at all the sites obtained with the method classical (right panel). Classical 1: Geopsy; Classical 2: Fäh et al., 2001; TFA1: wavelet-based time-frequency method as implemented in Geopsy software; TFA3: time-frequency method, Poggi and Fäh, 2010; Raydec: Hobiger et al., 2009. In the left panel picked resonance frequencies are indicated by red circles; the corresponding intervals are marked by red crosses.

The recordings from the passive sensors were also processed with the polarization tool of Burjanek et al. (2010). In Figure 9 we display the produced ellipticity (as defined in Burjanek et al., 2010) and strike/dip graphs as a function of frequency. The ellipticity plots (Figure 9, right) show a trough at 0.7 Hz and also a second one at 8-10 Hz, which correspond to the H/V peaks in Figure 8. For the polar strike (Figure 9, left), a moderate directionality effect can be identified for the 0.75 Hz peak along the NE-SW direction. This effect is more evident in ONU008 and the direction seems to be coincident with the main axis of the Geneva basin.
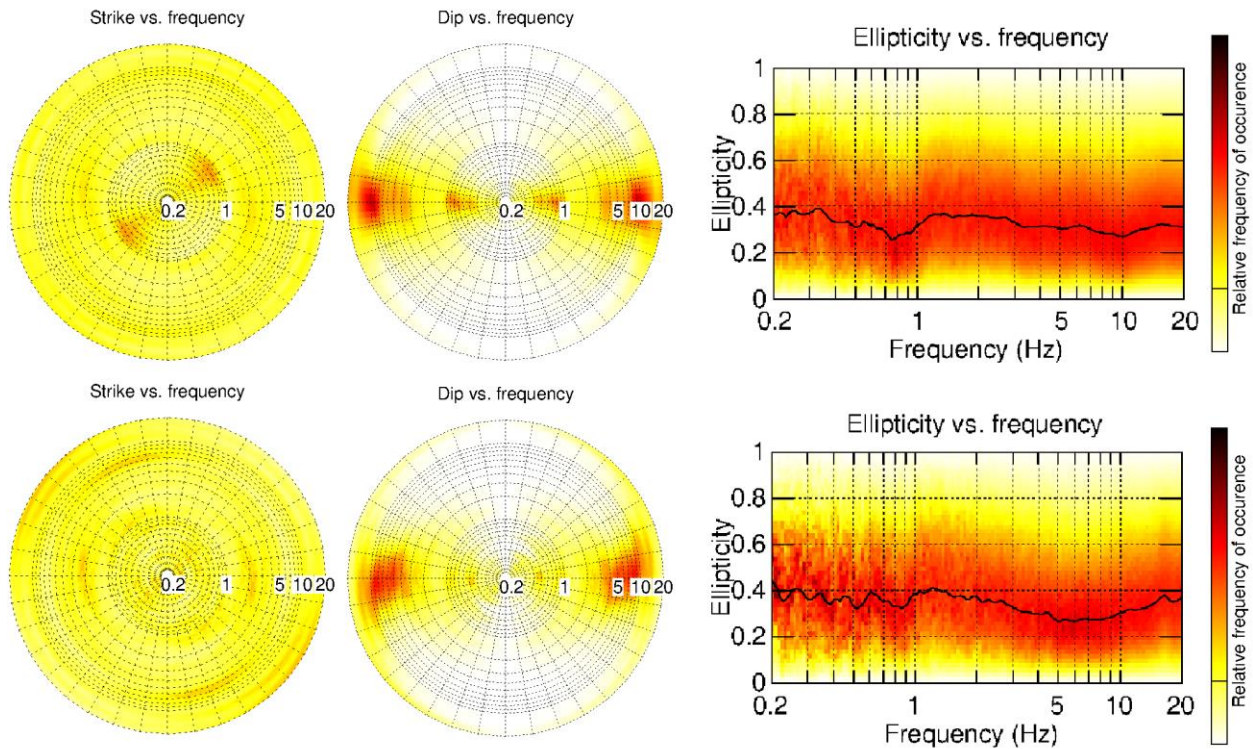
Figure 9 – Polarization analysis at the seismic station ONU008 (upper panels) and ONU002 (lower panels). From left to right, strike vs. frequency, dip vs frequency and ellipticity vs frequency graphs. Description on the computation method can be found in Burjanek et al. (2010).

5 Inversion of surface wave data

The Rayleigh wave dispersion and ellipticity curves obtained from the processing of active and passive seismic data were inverted for the 1D S-wave velocity profile of the investigated site. For the inversion the dinver code implemented in Geopsy (Wathelet et al., 2020) was used. The code provides a set of Vp/Vs models compatible with the observed dispersion curve. This inversion tool uses a directed-search method, called "neighbourhood algorithm" (Sambridge, 1999).

5.1 Inversion target

The target we selected for the inversion (Figure 10) consists of:

– The Rayleigh wave dispersion curve, as obtained from the processing of active data with the *f-k* processing. The forward and reverse shots curves are the same and for this reason Forward dispersion curve was used for the analysis because it covers a wider range of frequencies;

– The Rayleigh wave ellipticity curve from ONU008 single-station passive recording processed with Raydec between 2 and 20 Hz was considered.
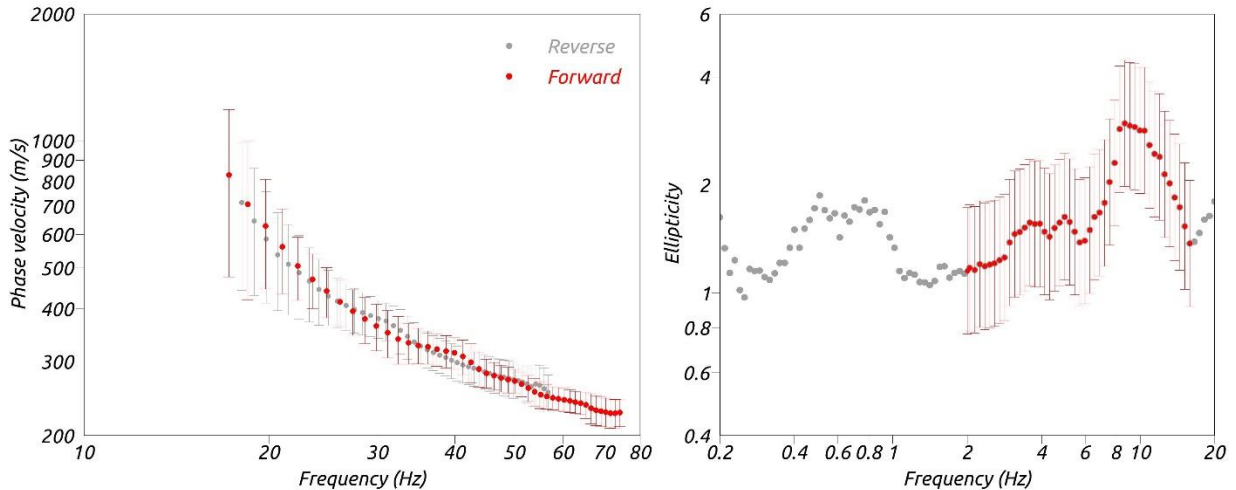
Figure 10 – Target of surface wave dispersion and ellipticity curves for the inversion process. Left: Rayleigh wave dispersion curve obtained from the processing of active data with f-k processing. Right: ellipticity curve for the fundamental mode of Rayleigh wave was obtained by processing passive data (ONU008) with Raydec code.

5.2 Parameterization of the model space

For the parameterization of the subsurface model two different strategies were followed: the soil column was modelled as a stack of 3 to 7 homogeneous layers overlying an halfspace and as 18 homogeneous layers with fix thickness. In both parameterizations at each layer the V_S can vary within broad boundaries (50-1500 m/s). The same applies to V_P (100-4000), although the resulting V_S/V_P ratio must be compatible with a range of possible values of Poisson's ratios set for each layer: $0.2 - 0.4$. The density values are attributed to each layer as equal to 1.9 t/m^3 and 2.0 t/m^3 for the halfspace. For each parameterization we completed an inversion run with $2x10^5$ models.

5.3 Inversion results

We performed a total of 6 inversions with different number of layers (see Table 1) using the Dinver routine (http://www.geopsy.org/). Each inversion run produced 200000 total models in order to assure a good exploration and exploitation of the parameter space. The results of these inversions are shown in Figs 11–15. The 5-layer parametrization yields slightly lower misfit values (Tab. 1), however the velocity profiles are generally consistent. The data fit is reasonably good for both surface wave dispersion and ellipticity curves.

Table 1: List of inversions

Inversion	Number of layers	Number of models	Minimum misfit
SONUG4l	4	200000	0.2099
SONUG5l	5	200000	0.2034
SONUG6l	6	200000	0.2142
SONUG7l	7	200000	0.2784
SONUGfix	19	200000	0.2519
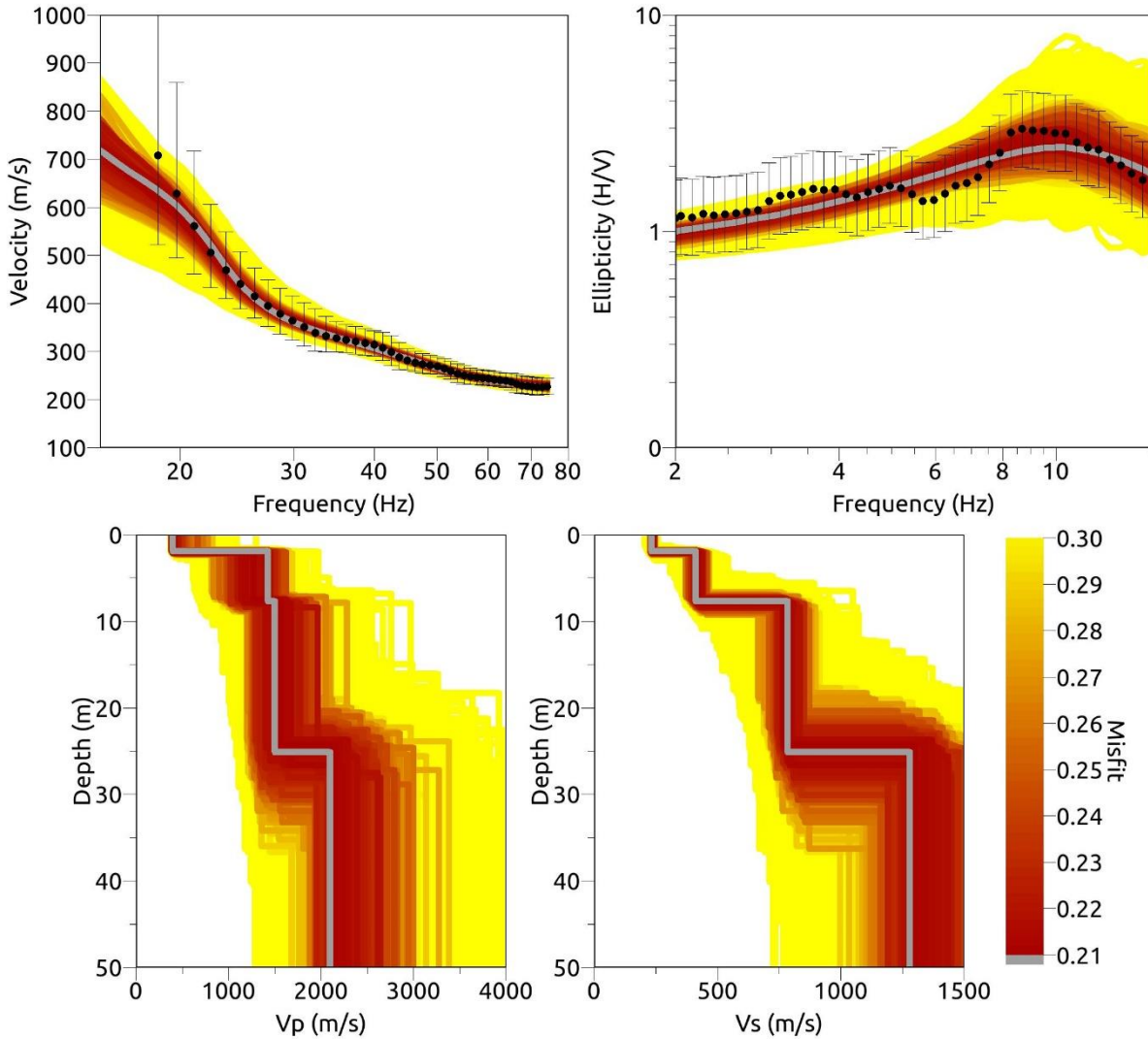
Figure 11: Inversion SONUG4l. Upper line: dispersion curves for the Rayleigh waves and ellipticity curve. Lower line: P-wave velocity profiles and S-wave velocity profiles. The black dots indicate the data points used for the inversion. The grey line indicates the best-fitting model.
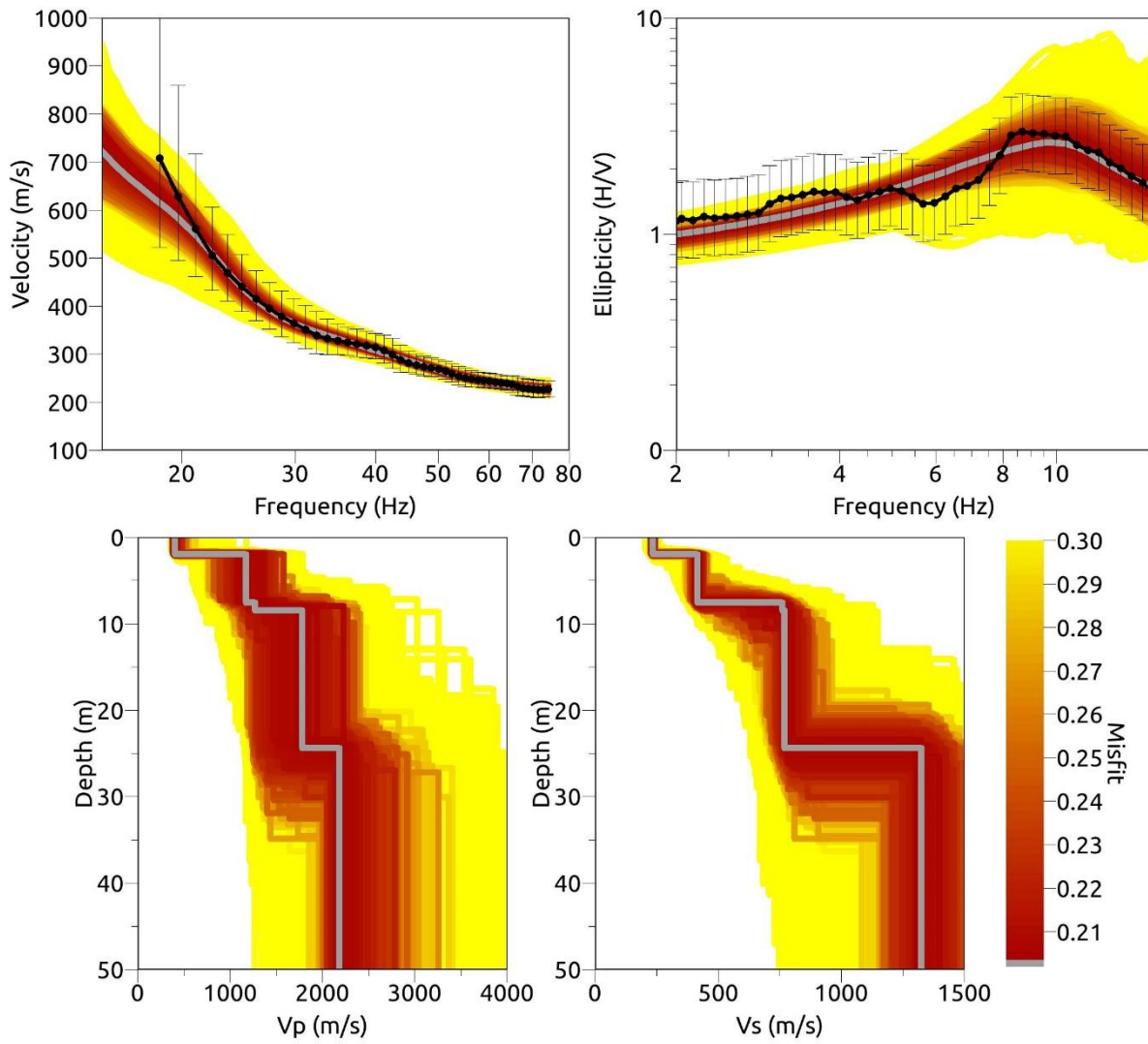
Figure 12: Inversion SONUG5l. Upper line: dispersion curves for the Rayleigh waves and ellipticity curve. Lower line: P-wave velocity profiles and S-wave velocity profiles. The black dots indicate the data points used for the inversion. The grey line indicates the best-fitting model.
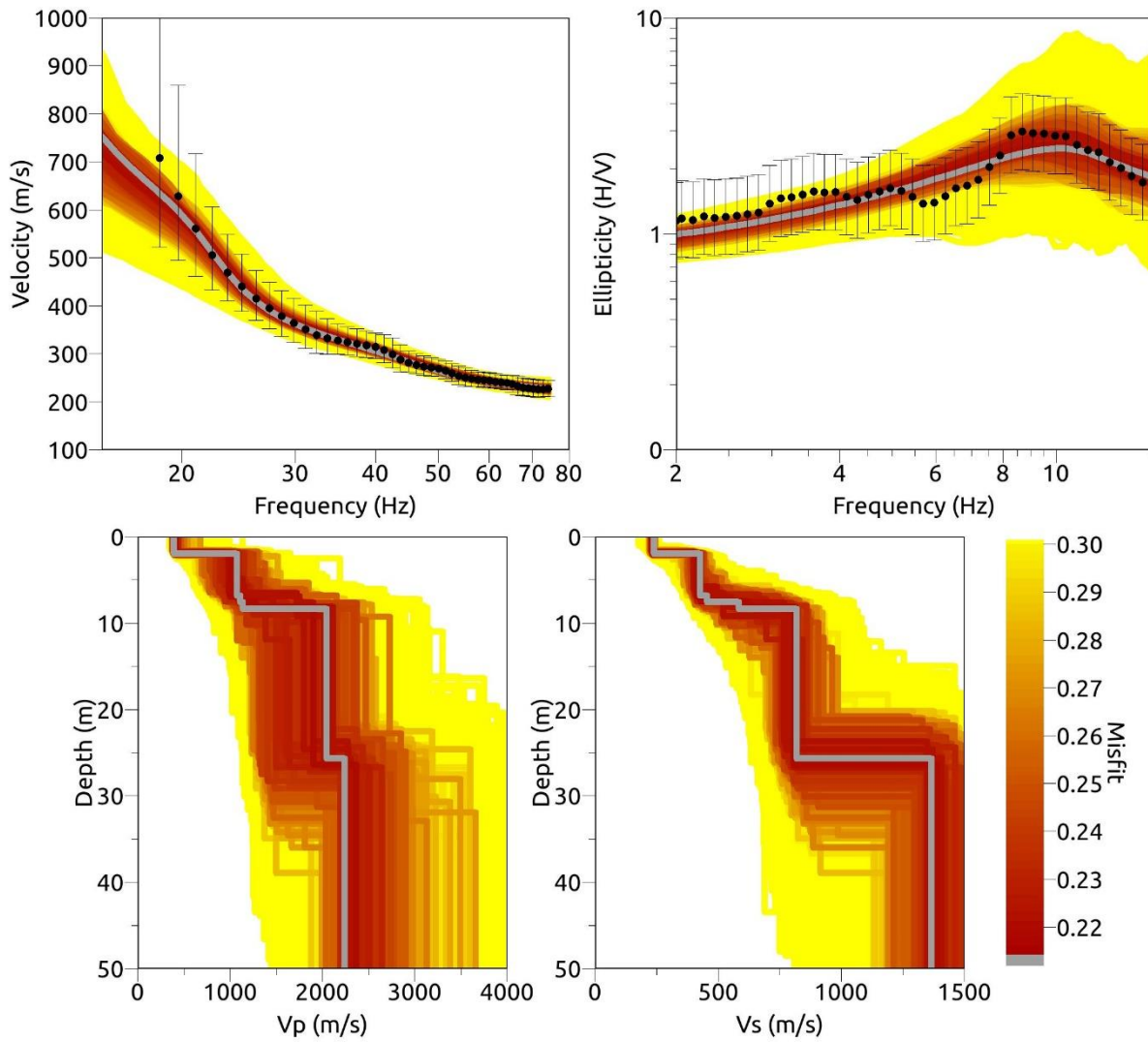
Figure 13: Inversion SONUG6l. Upper line: dispersion curves for the Rayleigh waves and ellipticity curve. Lower line: P-wave velocity profiles and S-wave velocity profiles. The black dots indicate the data points used for the inversion. The grey line indicates the best-fitting model.
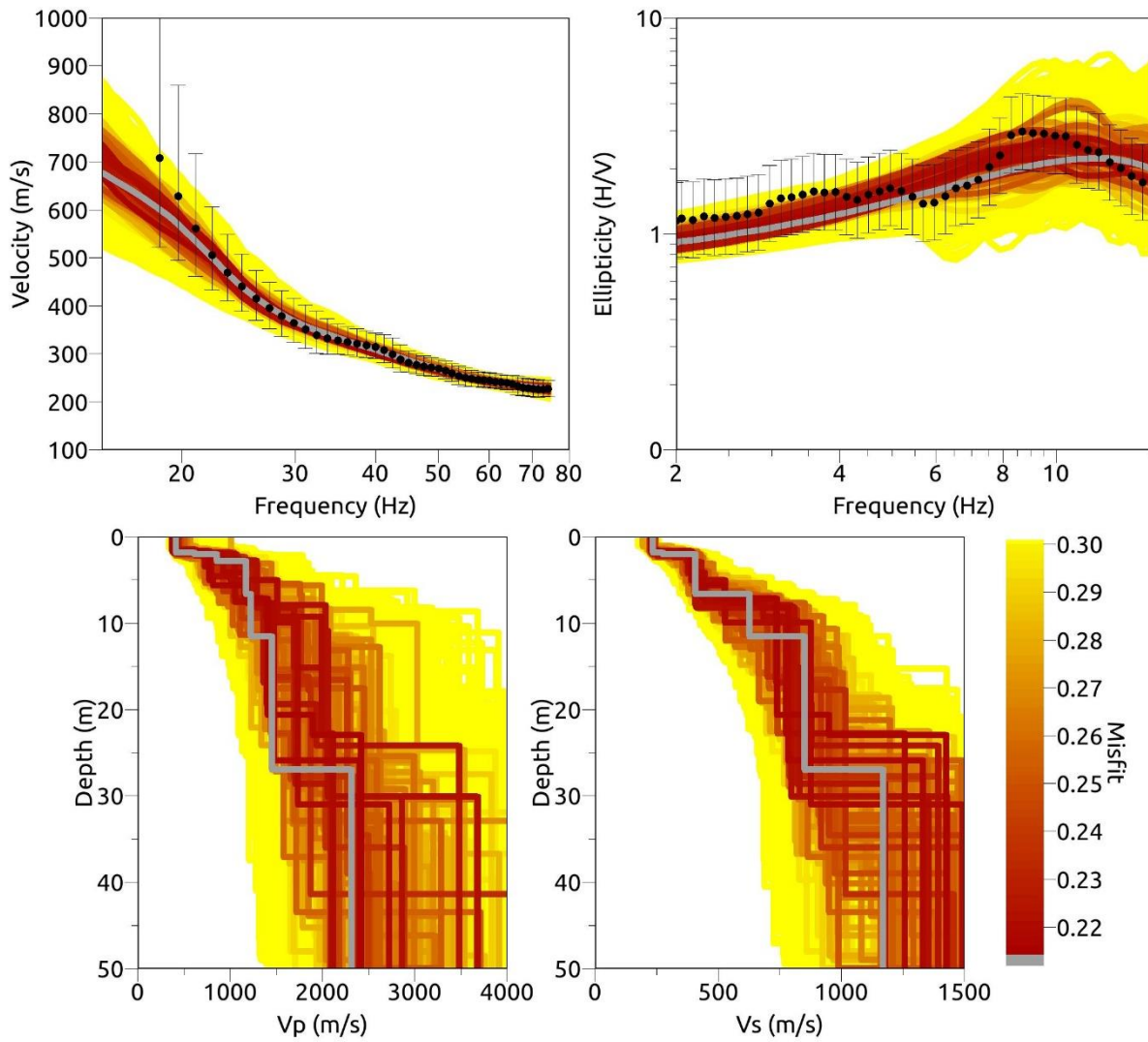
Figure 14: Inversion SONUG7l. Upper line: dispersion curves for the Rayleigh waves and ellipticity curve. Lower line: P-wave velocity profiles and S-wave velocity profiles. The black dots indicate the data points used for the inversion. The grey line indicates the best-fitting model.
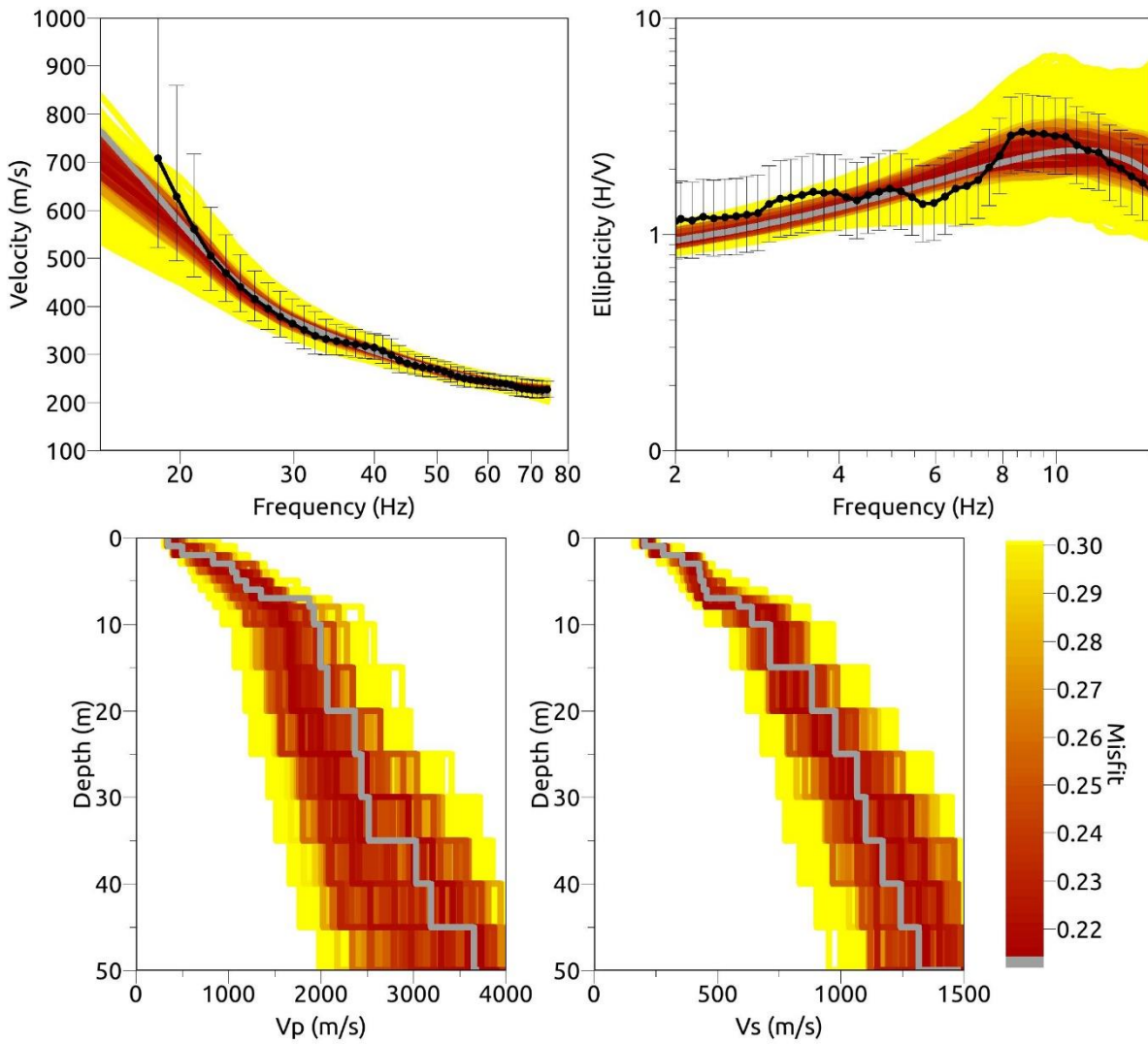
Figure 15: Inversion SONUGfix. Upper line: dispersion curves for the Rayleigh waves and ellipticity curve. Lower line: P-wave velocity profiles and S-wave velocity profiles. The black dots indicate the data points used for the inversion. The grey line indicates the best-fitting model.

7 Interpretation of the velocity profiles

7.1 Velocity profiles

The 6 best performing (i.e. lowest misfit) models from chosen layer parametrization inversions are considered as final result (Figure 16).

The upper 2 m have a V_S around 200 m/s, and they are presumably composed of weathering soil. Below, we observe two velocity layers, with thicknesses of around 5 and 20 m, and S-wave velocity increasing from 400 to 800 m/s; these layers should correspond to the moraine formation indicated by the geological map (Figure 2). At a depth of ~25 m, S-wave velocity increases to about 1300 m/s, but this velocity contrast is not recognized with a clear peak in the H/V curve, indicating probably that a gradually increase with depth rather than a sharp velocity contrast.
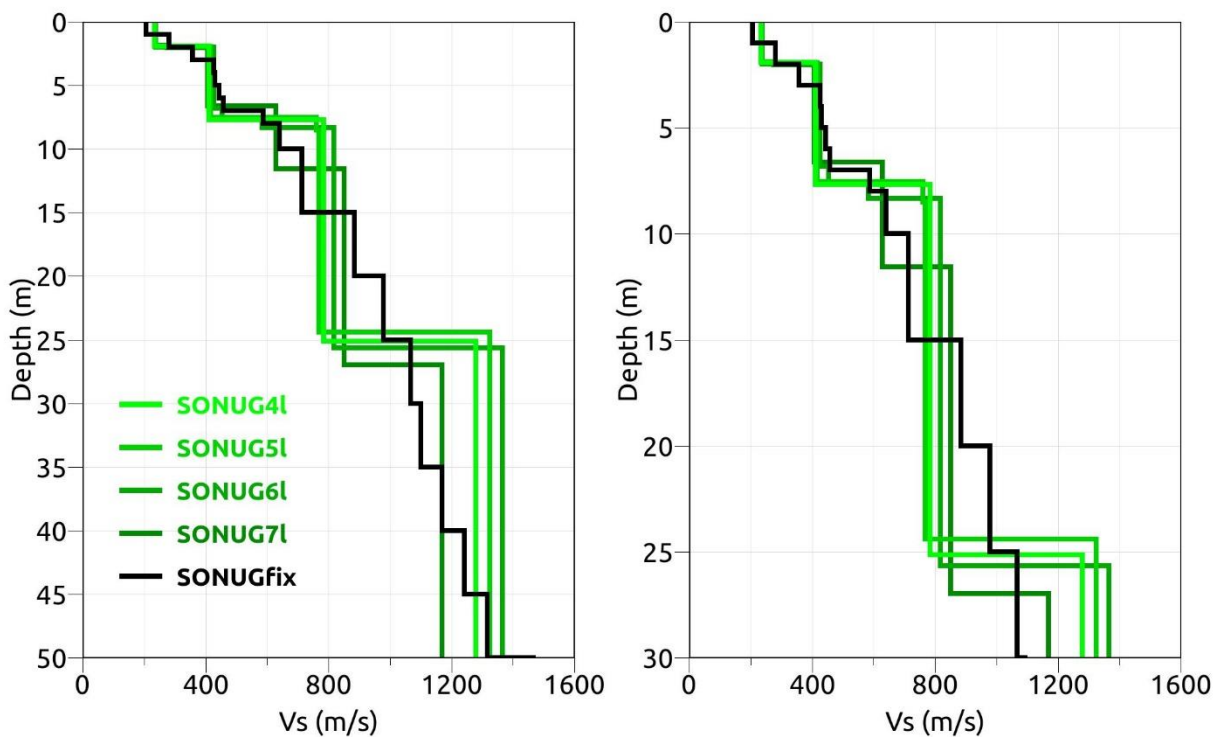
Figure 16: Overview of the best shear-wave velocity profiles of the different inversions for V_S (left) and for the V_S in the first 30 m (right).

7.2 Quarter-wavelength representation

The quarter-wavelength velocity approach (Joyner et al., 1981) provides, for a given frequency, the average velocity at a depth corresponding to 1/4 of the wavelength of interest. The results using this proxy, considering frequency limits of the experimental data is well constrained above 30 m (Fig. 17). The quarter wavelength impedance-contrast introduced by Poggi et al. (2012) is also displayed in the figure. It corresponds to the ratio between two quarter-wavelength average velocities, respectively from the top and the bottom part of the velocity profile, at a given frequency.
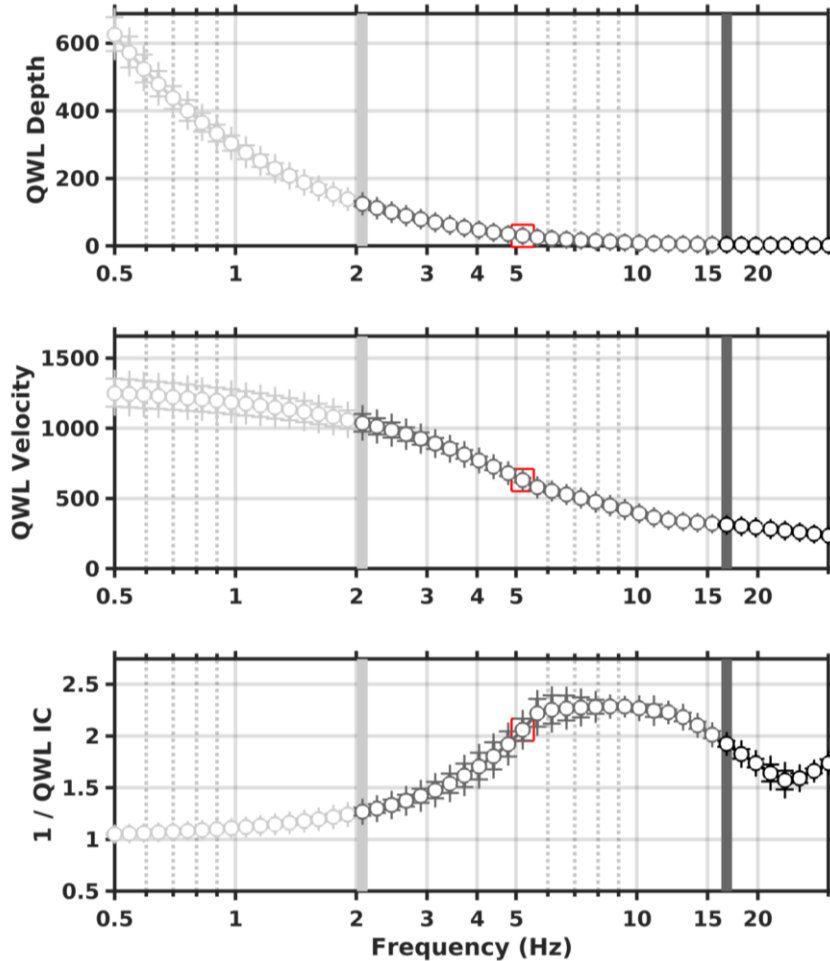
Figure 17: Quarter wavelength representation of the velocity profiles for the best models of the inversions (top: depth, center: velocity, bottom: inverse of the impedance contrast). The grey light bar shows the ellipticity lower frequency value, dark grey bar indicates the lower frequency value obtained with dispersion curves and red square corresponds to f_{30} (frequency related to the depth of 30 m).

7.4 Amplification function

In Figure 18, the average theoretical SH-amplification relative to the Swiss reference rock profile from the obtained models and adjusted ones are shown (black lines). In this case, the models are predicting an amplification up to a factor of 2.0 at frequency higher than 8.0 Hz, which is in quite good agreement with the peak observed in the empirical amplification function (red line). The present (28.01.2022) amplification from empirical spectral modeling (red line) is obtained using a maximum of 28 earthquakes recording. As soon as the station has recorded a sufficient number of earthquakes the comparison will be repeated.
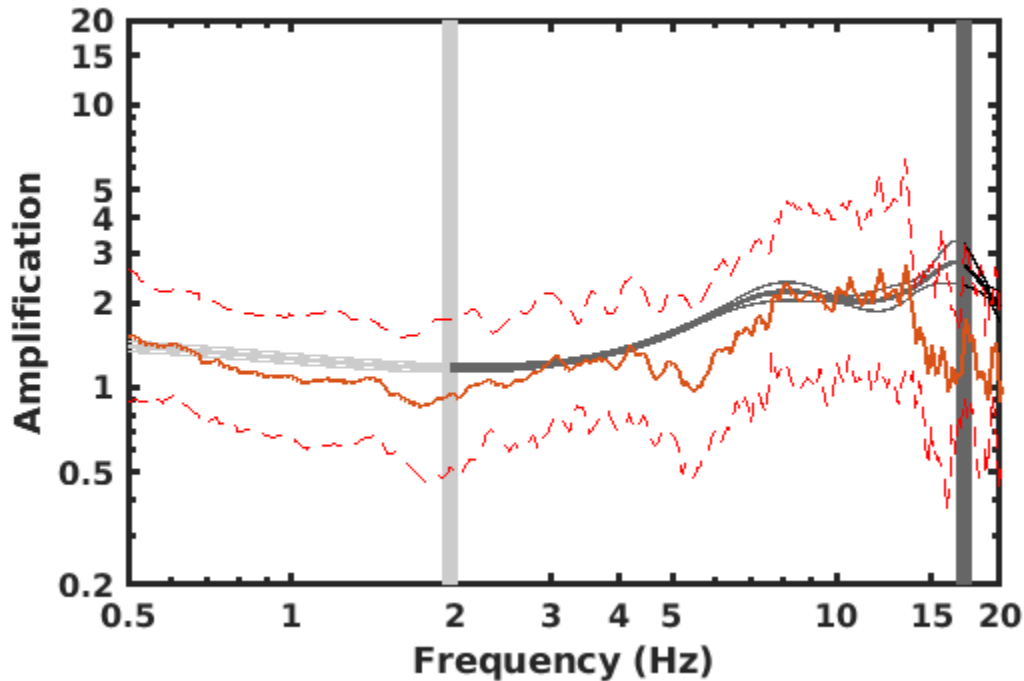
Figure 18: Modeled amplification function (black line) for the best velocity models of the five inversions. Red continuous line is the average empirical amplification function at the SONUG station, whereas dashed red lines are the standard deviations. Grey light bar show the minimum frequency of the ellipticity curve, whereas dark grey bar shows the minimum frequency obtained by dispersion curve.

6 Discussion and conclusions

The general HVSR amplitude at the station ONU008 (30 m far from SONUG) shows a bimodal low frequency peak between 0.4 and 1.0 Hz and a secondary peak at about 9.5 Hz. The low frequency bimodal peak could be explained as the resonance of Molasse deposits not resolved by our measurements, whereas the high frequency peak could be related to the artificial deposits outcropping in the area. A moderate directional effect is highlighted by polarization results at about 0.75 Hz with the NE-SW direction. This effect seems to be coincident with the main axis of the Geneva basin.

The inversion of the active seismic measurements yields a velocity profile with 3 main interfaces at about 2 m, 7 m and 25 m depth. In particular, the soft layer has a velocity of about 200 m/s, whereas the velocity of the below layers increase from 400 to 800 m/s reaching a velocity of about 1300 m/s at 25 m depth. The V_{S30} value of the site is determined as about 627 m/s, corresponding to soil class B in EC8 (CEN, 2004) and B in SIA261 (SIA, 2014) classifications. The theoretical SH-amplification relative to the Swiss reference rock profile predicts an amplification factor 2 at a frequency of 8.0 Hz, in quite good agreement with the amplification observations at this station.

Acknowledgements

References

Boiero, D., and L. V. Socco, 2010. Retrieving lateral variations from surface wave dispersion curves analysis: Geophysical Prospecting, 58, 977–996

Burjanek J., G. Gassner-Stamm, V. Poggi, J.R. Moore and D. Fäh, 2010. Ambient vibration analysis of an unstable mountain slope, GJI, 180, 820-828.

CEN, 2004. Eurocode 8: Design of structures for earthquake resistance – Part 1: general rules, seismic actions and rules for buildings. European Committee for Standardization, en 1998-1 edition.

Fäh, D., F. Kind, and D. Giardini, 2001. A theoretical investigation of average H/V ratios. GJI, 145, no. 2, 535-549.

Hobiger, M., P.-Y. Bard, C. Cornou, and N. Le Bihan, 2009. Single station determination of Rayleigh wave ellipticity by using the random decrement technique (Raydec). GRL, 36, L14303

Joyner, W. B., Warrick, R. E., and Fumal, T. E., 1981. The effect of Quaternary alluvium on strong ground motion in the Coyote Lake, California, earthquake of 1979. Bulletin of the Seismological Society of America, 71(4):1333–1349.

Kvaerna, T., and F. Ringdahl, 1986. Stability of various f-k estimation techniques. Semmiannual technical summary, 1 October 1985 – 31 March 1986, NORSAR Scientific Report, 1-86/87, Kjeller, Norway, 29-40.

Moscariello, A., 2019. Exploring for geo-energy resources in the Geneva Basin (Western Switzerland): opportunities and challenges. Swiss Bulletin für angewandte Geologie. 2019, 24, 2, 105-124.

Nakamura, Y., 1989. A Method for Dynamic Characteristics Estimation of Subsurface Using Microtremor on the Ground Surface. Quarterly Report of RTRI, vol. 30, no. 1, 25- 33.

Neducza, B., 2007, Stacking of surface waves: Geophysics, 72, 51–58.

O'Neill, A., 2003, Full-waveform reflectivity for modelling, inversion and appraisal of seismic surface wave dispersion in shallow site investigations: PhD thesis, University of Western Australia, Perth, Australia.

Park, C. B., R. D. Miller, and J. Xia, 1999. Multichannel analysis of surface waves: Geophysics, 64, 800–808.

Poggi, V., B. Edwards and D. Fäh, 2012. The quarter-wavelength average velocity: a review of some past and recent application developments. 15th WCEE, Lisbon 2012.

Poggi, V., and D. Fäh, 2010. Estimating Rayleigh wave particle motion from three component array analysis of ambient vibrations. GJI, 180, no. 1, 251-267.

Sambridge, M., 1999. Geophysical inversion with a neighbourhood algorithm—I. Searching a parameter space, Geophysical Journal International, 138(2), 479–494, https://doi.org/10.1046/j.1365-246X.1999.00876.x

SIA, 2014. SIA 261 Einwirkungen auf Tragwerke. Société Suisse des ingénieurs at des architectes, Zurich, Switzerland.

Socco, L.V., D. Boiero, S. Foti, and R. Wisen, 2009. Laterally constrained inversion of ground roll from seismic reflection records: Geophysics, 74, no. 6, G35-G45.

Swisstopo, Service géologique national, 2011. Atlas géologiques de la Suisse 1:25000 : LK 1048 feuille de Rheinfelden.

Wathelet, M., Chatelain, J.L., Cornou, C., Di Giulio, G., Guillier, B., Ohrnberger, M., Savvaidis, A., 2020. Geopsy: A User-Friendly Open-Source Tool Set for Ambient Vibration Processing. Seismological Research Letters, 91(3), 1878–1889, https://doi.org/10.1785/0220190360